Nanoscale

ROYAL SOCIETY OF CHEMISTRY

PAPER

View Article Online
View Journal | View Issue

Cite this: *Nanoscale*, 2024, **16**, 19704

Active site-exposed Bi_2WO_6@BiOCl heterostructures for photocatalytic hydrogenation of nitroaromatic compounds†

Le Liao, Guanshun Xie, Changqiang Yu, Zhaohui Huang, Senlin Zhang, Tongzheng Zhang, Xiuqiang Xie * and Nan Zhang *

Constructing heterostructured photocatalysts with highly exposed active sites proves to be an efficient strategy to improve the photocatalytic performance of bismuth-based photocatalysts. In this work, active site-exposed Bi_2WO_6@BiOCl (BWO@BOC) heterostructure composites based on two bismuth-based materials were fabricated by an *in situ* growth method for improving the photocatalytic hydrogenation of 4-aniline (4-NA) to *p*-phenylenediamine (PPD). BWO@BOC exhibited enhanced photoactivity for 4-NA hydrogenation compared to pure BWO and BOC. The optimal BWO@BOC composites displayed the highest conversion rate of 4-NA to PPD up to 99.3% within 12 min, with an apparent reaction rate constant of 0.414 min^{-1}, which is 3.3 times that of pure BOC. The photoactivity enhancement is mainly ascribed to the construction of a tight Z-scheme heterostructure with improved light harvesting properties and charge carrier transport efficiency, which were revealed by optical and photoelectrochemical characterization, respectively. Furthermore, the products of the hydrogenation process were monitored by *in situ* diffuse reflectance infrared Fourier transform spectroscopy (DRIFTS) to gain a better insight into the 4-NA hydrogenation mechanism.

Received 14th August 2024,
Accepted 23rd September 2024

DOI: 10.1039/d4nr03346a

rsc.li/nanoscale

1. Introduction

Aminobenzenes are crucial intermediates for industrial chemical synthesis. *p*-Phenylenediamine (PPD), one of the aminobenzenes, can be applied to prepare dyestuffs, medicines, resins, and rubber vulcanization accelerators.[1–3] Industrially, PPD can be directly prepared through the catalytic reduction of 4-nitroaniline (4-NA), which is one of the well-known methods for the synthesis of PPD.[4] However, the traditional catalytic 4-NA reduction process is complicated and highly costly due to the requirements of high temperature and high-pressure hydrogen.[5] Recently, photocatalytic conversion of 4-NA driven by solar energy under moderate conditions (room temperature in water) provides a promising alternative strategy for PPD synthesis,[6,7] which is in conformity with the principles of sustainability.

Bismuth-based materials such as Bi_2WO_6, $Bi_2Ti_2O_7$, $BiVO_4$, and BiOX (X = Cl, Br, and I) have garnered significant attention as photocatalysts for contaminant degradation and energy conversion owing to their chemical stability, non-toxicity, and good catalytic performance.[8–11] BiOCl (BOC) with its unique structure and electronic properties is studied as an alternative photocatalyst for photocatalytic 4-NA hydrogenation.[12] Its special sandwich-like crystal structure of a $[Bi_2O_2]^{2+}$ layer and double Cl^- layers is propitious for producing a built-in electric

College of Materials Science and Engineering, Hunan University, P. R. China.
E-mail: xiuqiang_xie@hnu.edu.cn, nanzhang@hnu.edu.cn

†Electronic supplementary information (ESI) available. See DOI: https://doi.org/10.1039/d4nr03346a

Nan Zhang

Nan Zhang is now a professor at the College of Materials Science and Engineering, Hunan University. She received her PhD in inorganic chemistry from Fuzhou University in 2016. She then worked in the Department of Electrical and Computer Engineering at the National University of Singapore as a postdoctoral fellow. Her main research interests include the design, optical property regulation and controlled fabrication of functional materials toward photocatalytic applications and their mechanism investigations.

field that can boost the separation and migration of photogenerated carriers.[11] Moreover, the hydrogen binding energy (ΔG_{H^*}) of the Bi element is determined to be ≈0.75 eV according to the theoretical computation of Nørskov and coworkers, which is higher than those of most commonly used elements such as Pt, Ag, and Pd.[13,14] The high ΔG_{H^*} suggests a strong interaction of H* with Bi, which is favorable for Bi to capture more H* to participate in the 4-NA hydrogenation reaction. However, the application of BOC is sensitively restricted by its poor light harvesting properties due to its broad bandgap (~3.3 eV).[15] The recent modification strategies for BOC photocatalysts include the fabrication of highly active crystal facet oriented BOC,[16] defect-rich BOC,[17,18] and ultrathin BOC nanosheets.[19] These strategies are based on single BOC. There exists a risk that crystal plane regulation and defect engineering may have adverse effects on the stability of materials.[20] Thus, constructing a heterostructure with another semiconductor is one of the effective strategies to improve the light absorption properties and charge separation efficiency while ensuring the stability of BOC photocatalysts.

As another bismuth-based material, Bi_2WO_6 (BWO) with a narrow bandgap of 2.6–2.9 eV is generally used as a visible light-responsive photocatalyst.[21] It also has a sandwich structure of a $[Bi_2O_2]^{2+}$ layer and a WO_4^{2-} octahedral layer, which is similar to BOC. The structural compatibility of BOC and BWO with shared $[Bi_2O_2]^{2+}$ can benefit electron transmission, which is favorable for the formation of a tight heterostructure.[22] Besides, the band potentials of BOC and BWO are well matched, which can facilitate the separation of photogenerated charge carriers at the interface of the heterojunction.[23,24] Therefore, constructing a coupled BOC/BWO heterostructure is regarded as a promising way to improve the performance of BOC photocatalysts. However, individual BWO exhibits no photoactivity for 4-NA reduction due to its insufficient reductive ability.[25] Thus, in this work, we designed an active site-exposed BWO@BOC heterostructure by using BWO as a platform to support the *in situ* growth of BOC nanosheets to improve the light absorption ability and spatial charge redistribution without sacrificing the active site of BOC. As compared to pure BWO and BOC, the as-prepared BWO@BOC composites showed enhanced photoactivity towards the hydrogenation reaction of nitroaromatic compounds under UV-vis light irradiation. The mechanism of photocatalytic 4-NA hydrogenation over BWO@BOC was studied through photoelectrochemical tests and especially *in situ* DRIFTS. This work is expected to provide more possibilities for the application of bismuth-based composites.

2. Experimental section

2.1. Preparation of BWO

BWO has been fabricated by a facile hydrothermal method.[24] Specifically, 4 mmol of $Bi(NO_3)_3{\cdot}5H_2O$ was first dissolved in 40 mL of deionized water to obtain solution A, and 3 mmol of Na_2WO_4 was then dissolved in 20 mL of deionized water to obtain solution B. Subsequently, solution B was added dropwise to solution A under continuous stirring for 2 hours. Following this, the mixed solution was transferred into a 100 mL Teflon-lined stainless-steel autoclave and heated at 180 °C for 12 hours. The resulting precipitate was collected by centrifugation, rinsed several times with deionized water and anhydrous ethanol, and then freeze-dried for 12 hours.

2.2. Preparation of BWO@BOC composites

2.2.1. Preparation of 0.15 M $BiCl_3$ solution. 37.5 mmol of $BiCl_3$ was dissolved in 210 mL of double-distilled water, followed by the addition of 24.6 mL of hydrochloric acid (36–38%) to the above solution. The mixed solution was stirred until $BiCl_3$ was fully dissolved at room temperature. Subsequently, the $BiCl_3$ solution was transferred to a 250 mL volumetric flask and diluted with a certain amount of distilled water to achieve a concentration of approximately 0.15 M.

2.2.2. Construction of BWO@BOC composites. For a typical BWO@BOC synthesis,[26] different masses of prepared BWO were preferentially added to 42 mL of distilled water and 50 mL of anhydrous alcohol and then sonicated for a few minutes until the BWO was well dispersed. Subsequently, 0.01 g of PVP (K30) and 1.20 mmol of citric acid monohydrate (CA) were added to the BWO-dispersed solutions. Then the above solutions were heated to 80 °C for about 5 minutes, and 8 mL of 0.15 M $BiCl_3$ solution was dropwise added to the solutions with continuous stirring at 80 °C for 3 hours. After the reaction was completed, the precipitates were collected by centrifugation, washed several times with deionized water and anhydrous ethanol to remove residual ions from the products, and then freeze-dried for 12 hours. The obtained powders with different mass ratios of BWO were named *x*-BWO@BOC (where *x* represents the weight ratio of 5%, 10%, and 15% of BWO to BOC, with *x* values being 5, 10, and 15, respectively). For comparison, pure BOC was also prepared through the same procedure, except for the addition of BWO.

2.3. Material characterization

The X-ray diffraction (XRD) patterns of the prepared samples were obtained using a MiniFlex 600 X-ray diffractometer (Rigaku, Japan) with Ni-filtered Cu Kα radiation at an accelerating voltage of 40 kV, a current of 20 mA, and a scan rate of 10° min^{-1}. Scanning electron microscopy (SEM, Hitachi S-4800, Japan) was used to observe the morphology of the prepared samples. X-ray photoelectron spectroscopy (XPS) spectra were recorded by using an AXISSUPRA spectrometer, with all binding energies calibrated using the C 1s peak at 284.8 eV. Ultraviolet–visible diffuse reflectance spectroscopy (UV-vis DRS) spectra were recorded using a UV-1780 spectrophotometer (Shimadzu, Japan). *In situ* diffuse reflectance infrared Fourier transform spectroscopy (DRIFTS) was conducted using a Nicolet iS50 FTIR spectrometer (Thermo Fisher, USA).

2.4. Photoelectrochemical measurements

Photoelectrochemical measurements were performed in a conventional three-electrode cell using an electrochemical

workstation (CHI600E, Shanghai Chenhua) with an Ag/AgCl electrode as a reference electrode and a Pt plate (10 mm × 10 mm) as a counter electrode. For preparing the working electrode, fluorine-doped tin oxide (FTO) glass was utilized as the substrate and ultrasonically washed with anhydrous ethanol for 30 minutes and then dried at 60 °C. Then Scotch tape with a 0.25 cm^2 hole was used to cover the conductive side of the FTO glass. 5 mg of the prepared samples were ultrasonically dispersed in 0.5 mL of *N*,*N*-dimethylformamide (DMF), and then 20 μL of the above suspension was spread on the hole near the end of the pretreated FTO glass. After drying naturally at room temperature, the Scotch tape was removed, and the uncoated section of the FTO glass was safeguarded with epoxy resin. The photocurrent and open circuit photovoltage (OCP) decay curves were recorded in a 0.2 M Na_2SO_4 aqueous solution under UV-vis light irradiation, performed using a 300 W Xe lamp system (PLS-SXE300+, Beijing Perfect Light Co., Ltd), without applied bias voltage. Electrochemical impedance spectroscopy (EIS) and cyclic voltammogram (CV) measurements were conducted in a 0.5 M KCl electrolyte containing 0.01 M $K_3[Fe(CN)_6]/K_4[Fe(CN)_6]$ under open-circuit potential conditions.

2.5. Photocatalytic activity tests

40 mg of catalyst and 40 mg of ammonium formate were added to 30 mL of nitroaromatic compound solution (20 ppm) in a glass reactor and then sonicated for several minutes until the catalyst was well dispersed. Before the light irradiation, the mixed solution was stirred for an hour in the dark to achieve adsorption–desorption equilibrium between the catalyst and reactant. The entire reaction process was carried out under Ar purging at a flow rate of 80 mL min^{-1}. During the light irradiation, 2 mL of suspension was collected at 2 minute intervals and filtered using polyethersulfone (PES) needle filters (0.22 μm) to remove the photocatalysts. The concentration of 4-NA was detected by using a UV-vis spectrophotometer (Shimadzu, UV-1780), and the conversion rate of 4-NA was calculated using the following eqn (1).

$$\text{Conversion } (\%) = (1 - C/C_0) \times 100\% \quad (1)$$

Furthermore, the reaction kinetics was studied using a pseudo-first-order kinetics model according to the following eqn (2).

$$-\ln(C/C_0) = kt \quad (2)$$

where C_0, C, and k represent the initial concentration of 4-NA, the concentration of 4-NA at time t during the reaction process, and the apparent rate constant, respectively.

3. Results and discussion

The BWO@BOC composites were synthesized by two-step hydrothermal-oil bath methods (as illustrated in Fig. 1a). First, BWO was prepared by a hydrothermal method. Then it was used as the substrate material, and PVP (K30) and citric acid monohydrate (CA) were used as synergistic structure-directing agents to support the *in situ* growth of BOC nanosheets on BWO through a refluxing process. For investigating the crystal phase and crystallinity of the prepared samples, XRD characterization was performed and the results are shown in Fig. 1b. It can be seen that all the characteristic peaks of pure BOC can

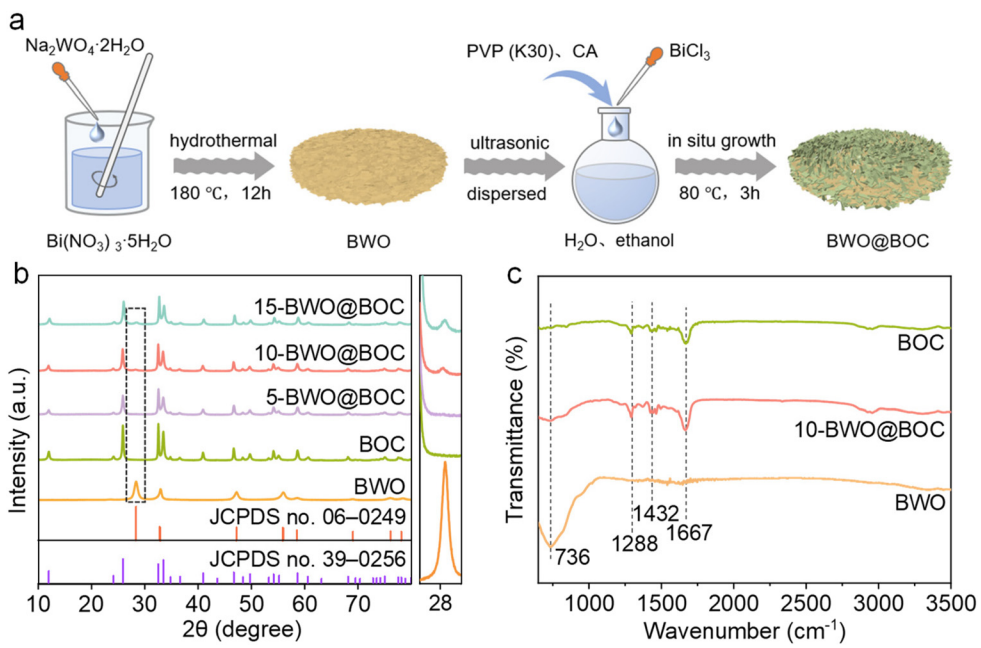

Fig. 1 (a) Scheme of the fabrication of BWO@BOC composites. (b) XRD patterns of the prepared samples. (c) FTIR spectra of BOC, 10-BWO@BOC, and BWO.

be assigned to the tetragonal BOC phase (JCPDS no. 39-0256). For the BWO@BOC composites, an additional characteristic peak at 28.3° originating from the orthorhombic BWO phase (JCPDS no. 06-0249) was detected, as shown in the enlarged view on the right side of Fig. 1b. Besides, the peak intensity at 28.3° increased with increasing the mass of BWO. This proved that the BWO@BOC composites were successfully prepared. No additional peak at 28.3° can be observed for 5-BWO@BOC, which should be ascribed to the low content of BWO. The Fourier transform infrared spectroscopy (FTIR) spectrum within the 650–3700 cm^{-1} range was analyzed to reveal the chemical construction of the prepared samples (as shown in Fig. 1c). For pure BOC, there were three distinct peaks at approximately 1288, 1432, and 1667 cm^{-1}, which can be attributed to the N–H–O complex, pyrrole, and C=O stretching vibrations, respectively.[27] Meanwhile in the BWO spectrum, a noticeable peak at 736 cm^{-1} was observed, corresponding to the W–O–W stretching mode.[28,29] The spectra of the 10-BWO@BOC composite displayed all the above characteristics peaks originating from pure BOC and BWO, confirming the successful formation of BWO@BOC composites.

SEM was employed to visually observe the microstructure of the prepared samples. As shown in Fig. 2a, bare BOC displayed a hollow flower-like structure with an average diameter of 1.65 μm (Fig. S1†), which was self-assembled from nanoflakes with a thickness of ~30 nm (Fig. S2†). Meanwhile, BWO presented a round pie-shaped structure (Fig. 2b) with an average size of 2.5 μm (Fig. S3†), which consisted of a large number of small nanosheets (Fig. S4†). Fig. 2c and Fig. S5† show the SEM image of 10-BWO@BOC, where BOC flakes can be seen interspersed on the surface of BWO with tight contact through the *in situ* growth method. Additionally, the corresponding elemental mapping patterns shown in Fig. 2d illustrated that the Bi, O, Cl, and W elements were uniformly distributed in the 10-BWO@BOC composite.

XPS was conducted to explore the chemical states of the samples and the electronic interaction between BWO and BOC. The Bi 4f spectrum (Fig. 3a) showed a pair of peaks of Bi^{3+} $4f_{7/2}$ and $4f_{5/2}$ at 159.2 and 164.5 eV for BOC and 158.6 and 163.8 eV for BWO. Noticeably, after the combination of BOC and BWO, the binding energy of 10-BWO@BOC located at 159.0 and 164.3 eV shifted negatively by ~0.2 eV compared with pure BOC, while it shifted positively by ~0.5 eV compared with pure BWO. This observation revealed the existence of interfacial interaction between BWO and BOC. To identify to which constituent the electron is directionally transferred, we also analyze the XPS signals of C1 2p and W 4f. The pair of peaks of the Cl 2p spectrum located at 197.9 and 199.5 eV for original BOC can be associated with Cl $2p_{3/2}$ and Cl $2p_{1/2}$ of Cl^- (Fig. 3b). After combining with BWO, the pair of peaks of Cl 2p were located at 197.7 and 199.3 eV, shifting to lower binding energy compared to original BOC, which implied an increased electron cloud density on the surface of BOC. In the W 4f spectrum of pure BWO (Fig. 3c), the pair of peaks at 34.8 and 36.9 eV well matched with the W $4f_{7/2}$ and W $4f_{5/2}$ of W^{3+}. After combining with BOC, the pair of peaks of W $4f_{7/2}$ and $4f_{5/2}$ were located at 35.0 and 37.1 eV, shifting to higher binding energy compared to the original BWO. This implied a decreased electron cloud density on the surface of BWO in the 10-BWO@BOC composite. Notably, the intensity of the W 4f

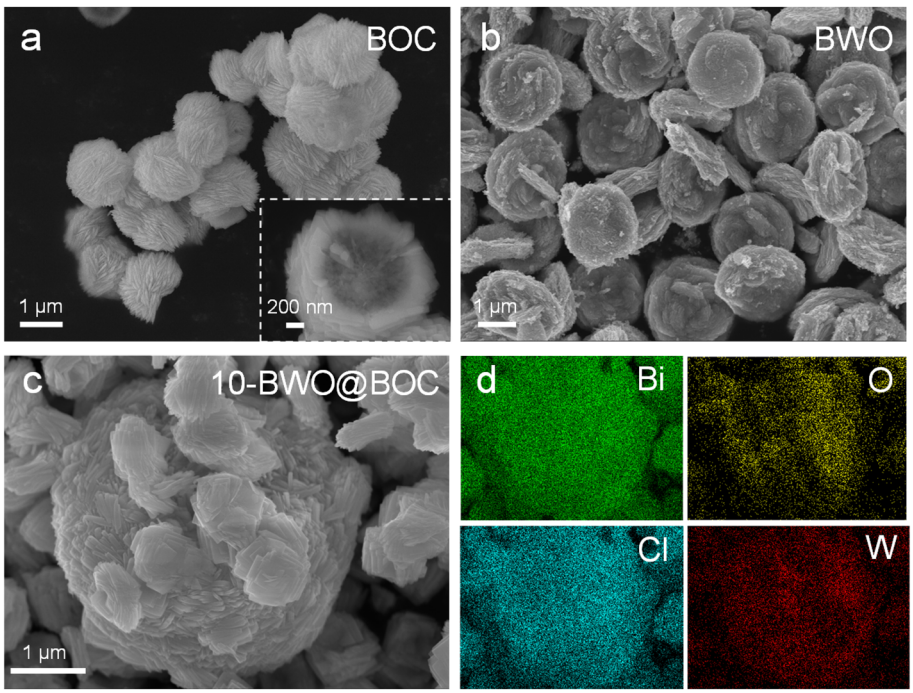

Fig. 2 SEM images of (a) BOC, (b) BWO, and (c) 10-BWO@BOC. (d) Mapping results for the included elements (Bi, O, Cl, and W) of 10-BWO@BOC.

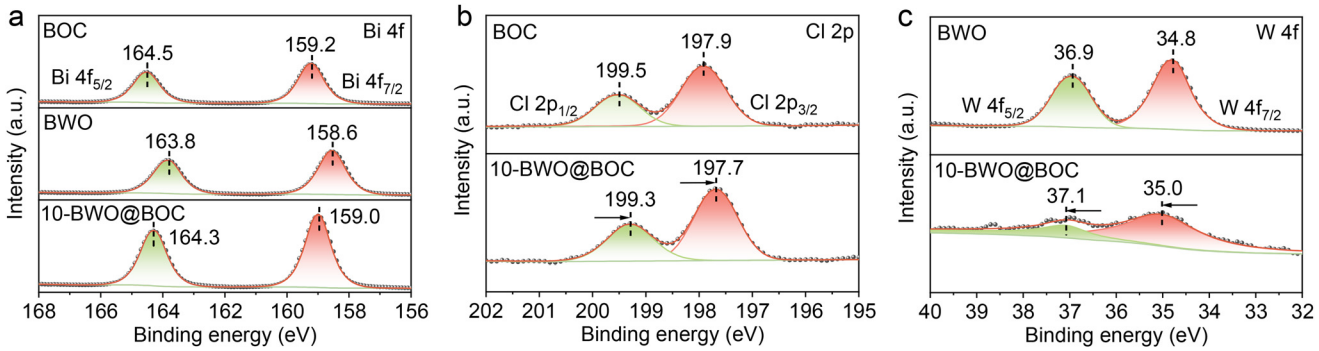

Fig. 3 XPS spectra of (a) Bi 4f, (b) Cl 2p, and (c) W 4f for BOC, 10-BWO@BOC, and BWO.

XPS spectrum for BWO@BOC was much weaker than that of BWO. This could be attributed to the low mass of BWO in the 10-BWO@BOC composite and the fact that BWO was surrounded by BOC nanosheets, which could attenuate the XPS signal of W. In brief, these XPS results indicated the effective transfer of electron cloud density from BWO to BOC after the formation of the BWO@BOC heterostructure.

The performance of BWO@BOC composites was evaluated by photocatalytic hydrogenation of 4-NA into PPD in the presence of ammonium formate as a hole sacrificial agent under UV-vis light irradiation (Fig. S6†). Fig. 4a displays the photocatalytic activity of the prepared samples. Pure BOC showed a 76.7% conversion rate of 4-NA hydrogenation while pure BWO exhibited almost no activity in the 4-NA reduction reaction due to its inadequate reductive potential (detailed discussion is presented in a later section). After the combination of BOC and BWO with different weight ratios, the 4-NA reduction capability of BWO@BOC composites was apparently improved compared to that of pure BOC and BWO. 10-BWO@BOC presented the highest 4-NA hydrogenation efficiency with a conversion of 4-NA to PPD of up to 99.3% within 12 min. Further increasing the BWO content to 15% resulted in the deterioration of 4-NA reduction performance over 15-BWO@BOC, indicating that the optimal weight ratio of BWO to BOC was 10% for BWO@BOC heterostructures. In addition, the mechanical mixing of the 10-BWO@BOC sample (denoted as 10-BWO@BOC-mix) was

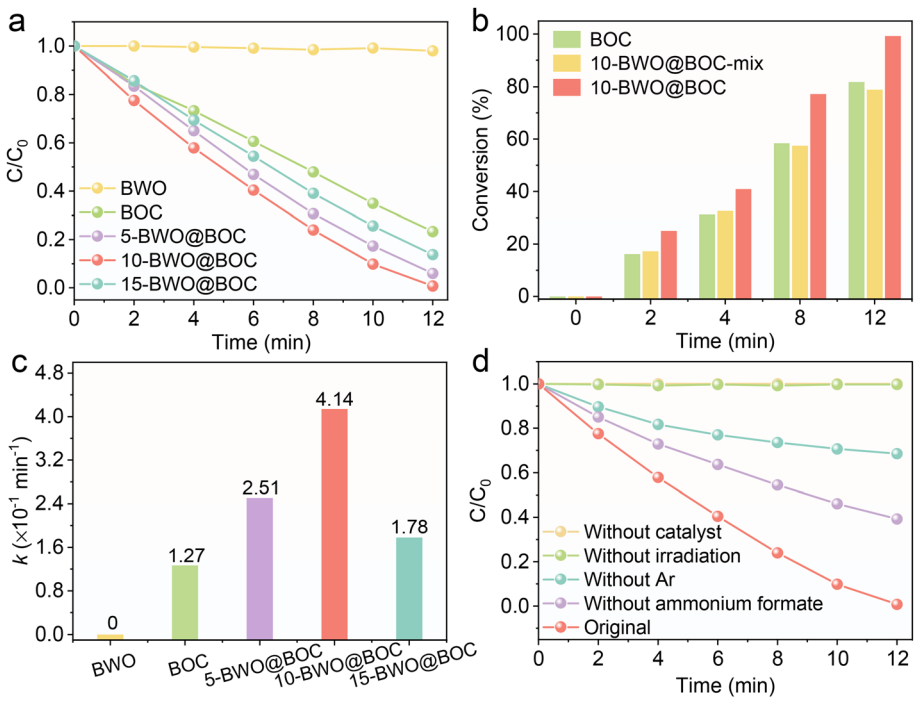

Fig. 4 (a) Photocatalytic performance of 4-NA hydrogenation over the prepared samples under UV-vis light irradiation with ammonium formate as a hole sacrificial agent. (b) Comparison of the 4-NA conversion rates of BOC, 10-BWO@BOC-mix and 10-BWO@BOC. (c) Corresponding apparent reaction rate constants obtained by fitting the pseudo-first-order kinetics model of the prepared samples. (d) Control experiments for the photocatalytic hydrogenation of 4-NA over 10-BWO@BOC.

also prepared. The photoactivity of 10-BWO@BOC-mix was obviously inferior to that of 10-BWO@BOC (Fig. 4b). This was due to the fact that BWO, which has no photoactivity for 4-NA hydrogenation, occupied some of the active sites of BOC. It highlighted the advantages of the *in situ* grown method for preparing the active site-exposed BWO@BOC heterostructures while emphasizing the significance of the interface interaction of the 10-BWO@BOC heterostructure.

To further quantitatively assess the 4-NA hydrogenation process over the prepared photocatalysts, the pseudo-first-order kinetics model was employed.[5,30] Fig. 4c depicts the corresponding apparent reaction rate constant of the prepared samples after fitting the pseudo-first-order kinetics model. It can be clearly observed that 10-BWO@BOC possessed the highest apparent reaction rate constant k of 0.414 min^{-1}, compared to BOC, 5-BWO@BOC, and 15-BWO@BOC with k values of 0.127 min^{-1}, 0.251 min^{-1}, and 0.178 min^{-1}, respectively.

Control experiments over 10-BWO@BOC were carried out to explore the mechanism of photocatalytic 4-NA hydrogenation (Fig. 4d). There was no conversion of 4-NA in the absence of catalysts and light irradiation, indicating that the photoactivity originated from the photocatalytic process. The hydrogenation rate of 4-NA markedly decreased without Ar bubbling, verifying that the inert atmosphere created by Ar bubbling was vital for the efficient photocatalytic hydrogenation of 4-NA. It was reported that ammonium formate as a hole sacrificial agent can easily quench photoinduced holes and produce $^{\bullet}CO_2^-$ radicals with strong reduction ability ($E_{(^{\bullet}CO_2^-/CO_2)}$ = −2.2 V *vs.* NHE, pH = 6.8), which can effectively reduce 4-NA to PPD ($E_{(4\text{-NA/PPD})}$ = −0.67 V *vs.* NHE).[5] As a result, the conversion of 4-NA decreased to 60.7% without adding ammonium formate, indicating that ammonium formate as a hole sacrificial agent efficiently promoted the separation of photogenerated electron–hole pairs and improved the reduction ability of photocatalysts.

In order to explore whether the enhanced photoactivity over 10-BWO@BOC is universal to nitroaromatic compounds, we have further investigated the photocatalytic performance of original BOC and 10-BWO@BOC towards the hydrogenation of several typical nitroaromatic compounds with different substituent groups, such as 4-nitrotoluene, 4-nitroanisole, 4-nitrochlorobenzene, and 4-nitrophenol (Fig. 5a–d). It could be seen that 10-BWO@BOC exhibited higher conversion of all four nitro compounds than the original BWO and BOC, which was similar to that for the transformation of 4-NA to PPD.

To achieve a deeper understanding of the mechanism behind the enhanced photoactivity over BWO@BOC composites, a series of photo-electrochemical measurements have been conducted. Fig. 6a depicts the on–off transient photocurrent density of the prepared samples. All BWO@BOC

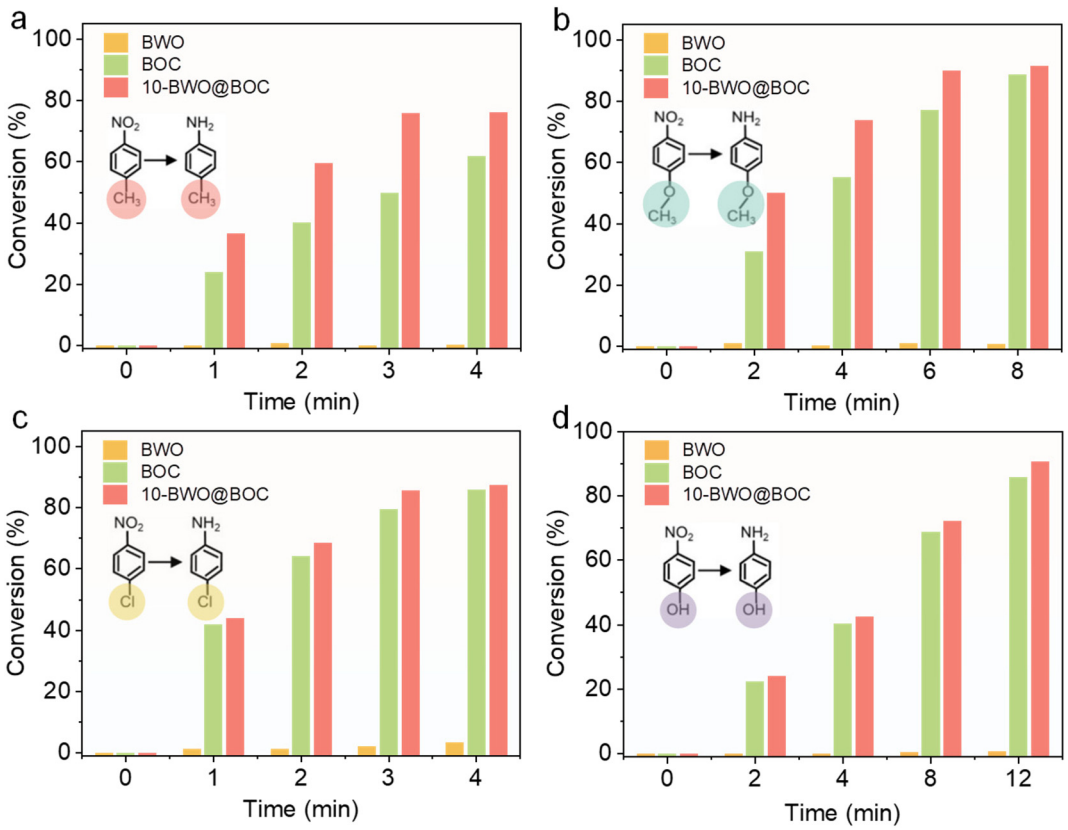

Fig. 5 Photocatalytic performance of BWO, BOC and 10-BWO@BOC for the hydrogenation of (a) 4-nitrotoluene, (b) 4-nitroanisole, (c) 4-nitrochlorobenzene, and (d) 4-nitrophenol.

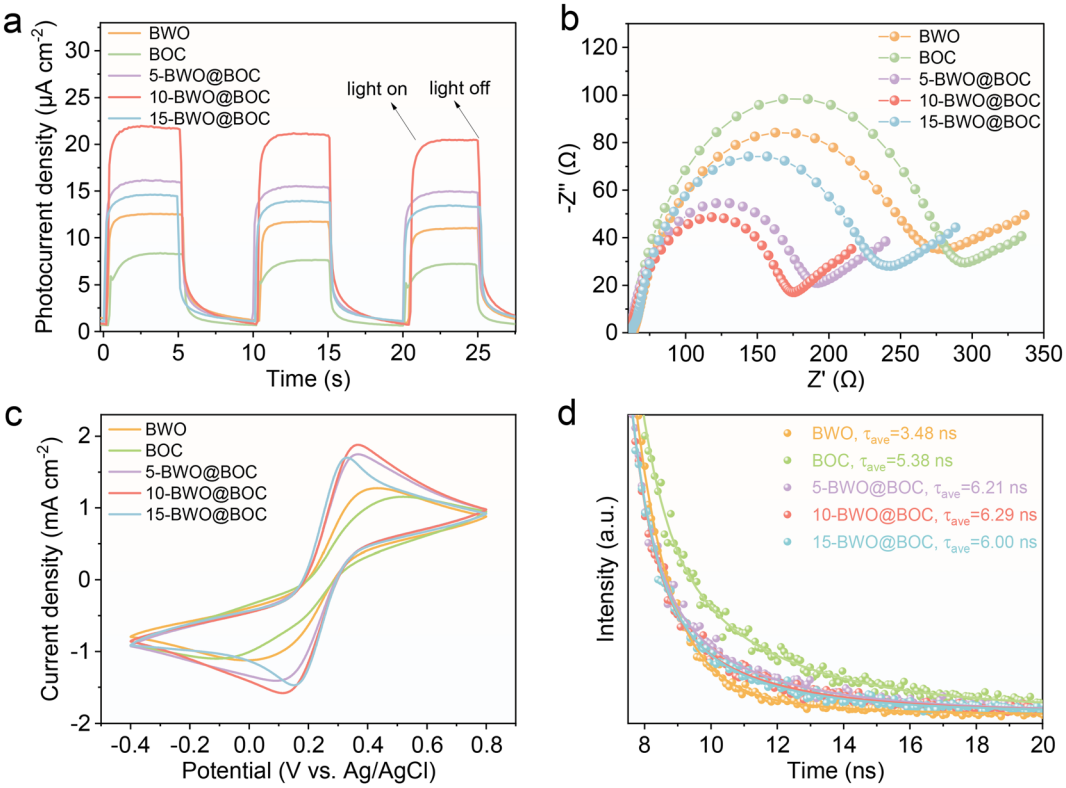

Fig. 6 (a) Photocurrent density under UV-vis light irradiation, (b) Nyquist plots, (c) CV curves, and (d) time-resolved transient photoluminescence (TRPL) spectra (obtained at an excitation wavelength of 370 nm) of the prepared samples.

composites with different BWO ratios exhibited higher transient photocurrent density in comparison with pure BOC and BWO, indicating that the formation of the BWO@BOC heterostructure promoted the separation and transfer efficiency of photoinduced carriers.[31,32] In addition, 10-BWO@BOC possessed the maximum photocurrent response, which was consistent with the catalytic performance results. Similarly, the Nyquist plots (Fig. 6b) illustrated that all BWO@BOC heterostructures displayed a depressed semicircle in contrast to pristine BOC and BWO, and 10-BWO@BOC showed the smallest semicircle among the BWO@BOC composites, further emphasizing the significant role of the BWO@BOC heterostructure in facilitating the carrier separation and migration.[33,34] This was also verified by the CV curves (Fig. 6c), where 10-BWO@BOC exhibited the highest current density compared to pure BOC, BWO, and other BWO@BOC composites. OCP decay measurements have also been conducted to study the photoexcited charge transfer kinetics as shown in Fig. S7a.† It could be seen that the 10-BWO@BOC photoelectrode exhibited the lowest open circuit potential. This was due to the fact that the accumulation of photoelectrons caused a shift in the Fermi level, which led to a more negative potential in the OCP.[35,36] On the other hand, Fig. S7b† shows the electron lifetime *vs.* potential plots derived from the OCP decay curves. It was observed that the 10-BWO@BOC photoelectrode possessed a longer photoelectron lifetime as compared to pure BWO and BOC, suggesting the lowest photoinduced carrier recombination rate of the 10-BWO@BOC photoelectrode.[36,37] Time-resolved transient photoluminescence (TRPL) spectroscopy was also performed to investigate the recombination situation of photoinduced electron–hole pairs. As shown in Fig. 6d and Table S1,† the average carrier lifetimes (τ_{ave}) of BWO, BOC, 5-BWO@BOC, 10-BWO@BOC, and 15-BWO@BOC were calculated to be 3.48, 5.38, 6.21, 6.29, and 6.01 ns, respectively. Compared to bare BWO and BOC, the extended τ_{ave} of BWO@BOC composites indicated that the formation of BWO@BOC heterojunctions suppressed the recombination of photogenerated charge carriers.[38,39] Among the samples, 10-BWO@BOC exhibited the most efficient suppression of the charge carrier recombination, which is consistent with its highest photoactivity.

The optical absorption properties and the energy band structure of pristine BOC, BWO, and 10-BWO@BOC have also been analyzed. According to UV-vis diffuse reflectance spectra (DRS) (Fig. 7a), the optical response range of BOC is mainly below 370 nm (ultraviolet range) due to its broad bandgap. As the mass of BWO increased, a slight red shift of the optical absorption edge was observed over the BWO@BOC composites. This red shift led to an improvement in light utilization, which favors the enhancement of the photocatalytic efficiency.

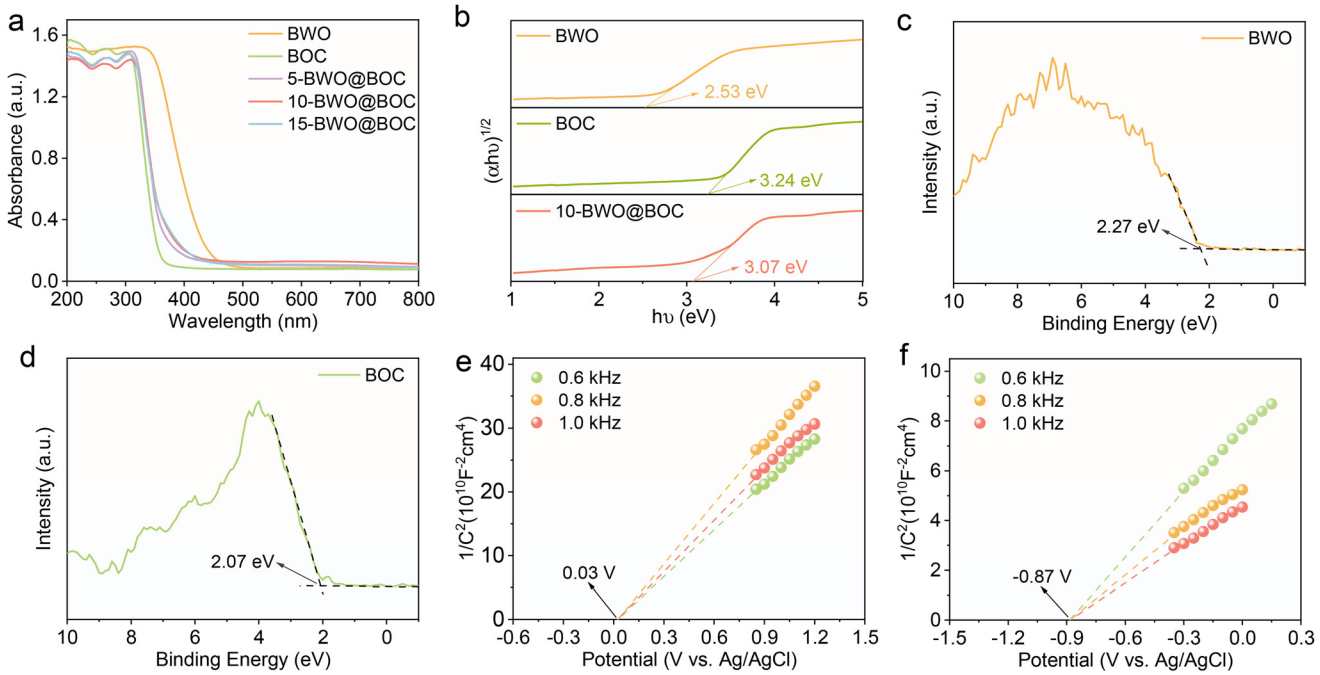

Fig. 7 (a) UV-vis DRS spectra of the prepared samples and (b) Tauc plots of BWO, BOC, and 10-BWO@BOC. Valence band XPS spectra of (c) BWO and (d) BOC. Mott–Schottky plots of (e) BWO and (f) BOC.

Fig. 7b shows the corresponding Tauc plots obtained from UV-vis DRS spectra *via* the Kubelka–Munk equation,[40] where the bandgap energies (E_g) of BWO, BOC, and 10-BWO@BOC were calculated to be 2.53, 3.24, and 3.07 eV, respectively. The combination of BWO and BOC narrowed the bandgap of the 10-BWO@BOC composites, enhancing their light harvesting properties. Besides, the valence band potential (E_{VB}) of the semiconductor can be obtained from valence band XPS (VB-XPS) spectra. As shown in Fig. 7c and d, the VB-XPS values of BWO and BOC were calculated to be 2.27 and 2.09 eV, respectively. The E_{VB} of the normal hydrogen electrode ($E_{VB\text{-}NHE}$, pH = 7) can be determined using the equation: $E_{VB\text{-}NHE} = \varphi + E_{VB\text{-}XPS} - 4.44$, where φ represents the electron work function (4.62 eV) of the XPS analyzer. Thus, the $E_{VB\text{-}NHE}$ values of BWO and BOC were calculated to be 2.45 and 2.27 eV, respectively. Combined with the above calculated E_g, the conduction band potential (E_{CB}) of BWO and BOC could be deduced using the equation $E_{CB} = E_{VB} - E_g$, resulting in values of −0.08 and −0.97 eV (*vs.* NHE, pH = 7), respectively. The less negative E_{CB} of BWO compared to the reduction potential of 4-NA/PPD (−0.67 eV *vs.* NHE) provided an explanation for the lack of photoactivity of BWO towards the 4-NA hydrogenation reaction. The Mott–Schottky plots of pure BWO and BOC electrodes have also been obtained as shown in Fig. 7e and f. The positive slopes of the Mott–Schottky (M–S) plots of BWO and BOC electrodes suggested the typical n-type semiconductor behavior of BWO and BOC.[41,42] Accordingly, the derived flat-band potentials (E_f) of BWO and BOC according to the M–S plots were −0.01 V and −0.87 V *vs.* Ag/AgCl at pH = 7, respectively. The above flat-band potentials ($E_{f,Ag/AgCl}$) could be converted to the normal hydrogen electrode ($E_{f,NHE}$, pH = 7) potentials according to the following equation:

$$E_{f,NHE} = E_{f,Ag/AgCl} + E^0_{AgCl}$$

where E^0_{AgCl} is 0.197 eV. Thus, the $E_{f,\ NHE}$ values of BWO and BOC were 0.19 and −0.67 eV, respectively. Generally, the E_{CB} of the n-type semiconductor was 0.1–0.3 eV negative than the $E_{f,NHE}$,[43] so the E_{CB} values of BWO and BOC were approximated to be 0.09 to −0.11 eV and −0.77 to −0.97 eV (*vs.* NHE, pH = 7), respectively. They were consistent with the above-mentioned CB potentials calculated using the Tauc plots and VB-XPS.

In situ DRIFTS of 4-NA adsorption in the dark for 20 min and a hydrogenation reaction under UV-vis light irradiation for another 20 min over 10-BWO@BOC were conducted to explore the hydrogenation mechanism. It can be seen from Fig. 8a and Fig. S8† that several peaks emerged when H_2O and 4-NA were introduced into the system in the dark. The peaks at 3448 and 1650 cm^{-1} were associated with the stretching and bending vibrations of the –OH group of H_2O, and the peaks at 3530, 2037, and 1621 cm^{-1} originated from the conjugated bonds of the aromatic ring skeleton.[44] Besides, characteristic absorption peaks at 1530 and 1350 cm^{-1} emerged, which were attributed to the asymmetric and symmetric stretching vibrations of the $-NO_2$ group, respectively.[45] These peaks exhibited heightened intensity as the adsorption time increased. Upon light irradiation, the intensity of peaks at 1530 and 1350 cm^{-1} decreased, indicating that the N–O bond of $-NO_2$ was broken, boosting the dissociation of the $-NO_2$ group.[45] Notably, a new

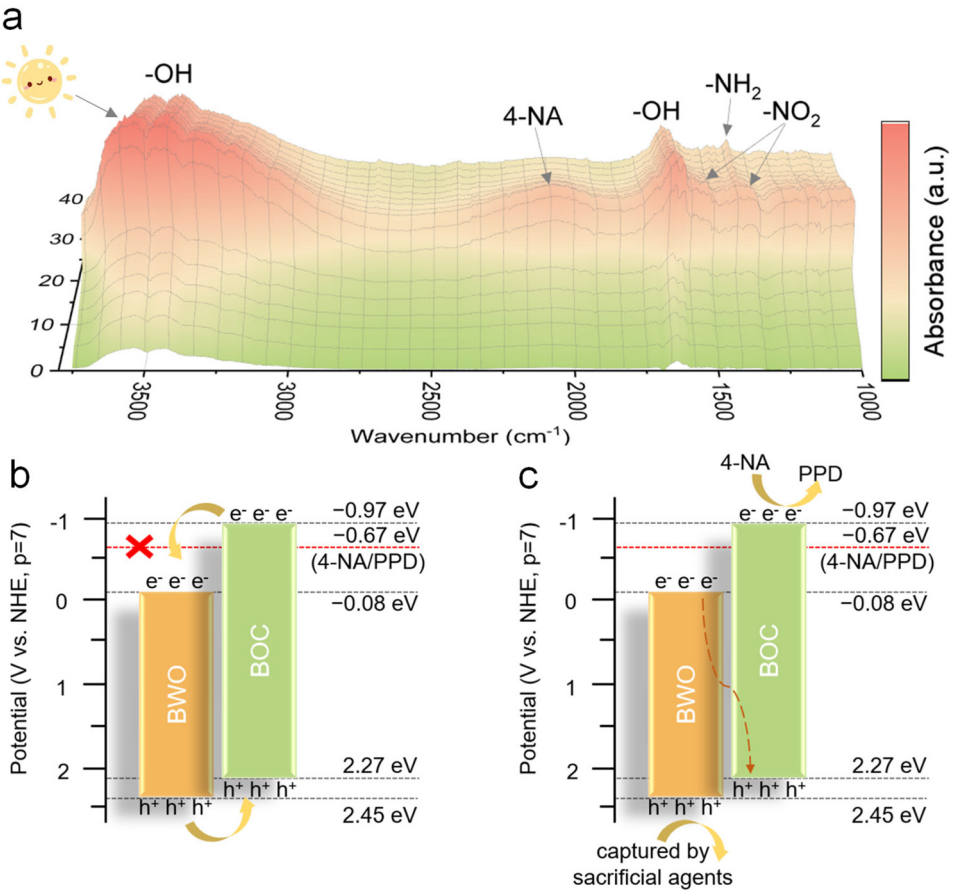

Fig. 8 (a) *In situ* DRIFTS spectra of 10-BWO@BOC for the adsorption of a mixture of H_2O and 4-NA for 20 minutes in the dark and under UV-vis light irradiation for another 20 minutes. The proposed charge transfer mechanism of (b) type-II and (c) Z-scheme heterostructures over the 10-BWO@BOC heterostructure for the photocatalytic hydrogenation reaction of 4-NA under UV-vis light irradiation.

peak at 1407 cm^{-1} can be observed, which belonged to the $-NH_2$ group of aniline,[46] indicating the production of PPD.

On the basis of the above-discussed energy band structures of BWO and BOC, the possible electron transfer mechanism of a type-II heterostructure or a Z-scheme heterostructure over the BWO@BOC heterostructure was proposed to explain the enhanced photoactivity for the 4-NA hydrogenation reaction. However, due to the less negative E_{CB} of BWO (−0.08 eV *vs.* NHE) than the reduction potential of 4-NA/PPD (−0.67 eV *vs.* NHE) (Fig. 8b), the CB electron of BWO should be incapable of reducing 4-NA to PPD from a thermodynamic perspective. This was experimentally confirmed by the result presented in Fig. 4a. Therefore, the transfer route of the photoinduced charge carriers followed the typical Z-scheme mechanism (Fig. 8c). The electrons were photoexcited from the VB to the CB of BWO and BOC under UV-vis light irradiation. Then the photoinduced electrons in the CB of BWO tend to directly recombine with the holes in the VB of BOC, leaving the electrons of BOC to reduce 4-NA to PPD, while the holes of BWO are captured by ammonium formate. This Z-scheme heterostructure effectively retarded the recombination of photogenerated electron–hole pairs while maintaining the robust reduction ability of BOC (−0.97 eV *vs.* NHE), thus enhancing the photoactivity of BWO@BOC composites towards the hydrogenation reaction of nitroaromatic compounds.

4. Conclusions

In summary, we have synthesized active site-exposed BWO@BOC heterostructures based on two bismuth-based materials (BWO and BOC) by an *in situ* growth method. The activities of the as-synthesized BWO@BOC heterostructures were evaluated through the photocatalytic hydrogenation reaction of 4-NA to PPD under UV-vis light irradiation. Compared to bare BWO and BOC, BWO@BOC composites exhibited enhanced photoactivities. Control experiments with the comparison of chemical and mechanical mixing preparation methods of 10-BWO@BOC illustrated the vital role of BWO@BOC heterostructures in facilitating the migration of photoinduced electron flow. Finally, an electron transfer route of Z-scheme heterojunctions for the coupled BWO/BOC semiconductors was proposed by experimental characterization

and band structure analysis to explain the enhanced photoactivity of BWO@BOC heterostructures.

Author contributions

L. Liao: methodology, conceptualization, investigation, formal analysis, data curation, writing of the original draft, and result discussion. G. Xie: investigation and editing. C. Yu: review and editing. Z. Huang: review and editing. S. Zhang: graphic design. T. Zhang: investigation and visualization. X. Xie: project administration, funding acquisition, validation, supervision, review, and editing. N. Zhang: project administration, funding acquisition, validation, supervision, review, and editing.

Data availability

The data that support the findings of this study are available from the corresponding author upon reasonable request.

Conflicts of interest

The authors declare no competing financial interest.

Acknowledgements

This work was supported by the National Natural Science Foundation of China (52272295, 52071137, 51977071, 51802040, and 21802020), the Science and Technology Innovation Program of Hunan Province (2021RC3066 and 2021RC3067), and the Natural Science Foundation of Hunan Province (2020JJ3004 and 2020JJ4192). N. Z. and X. X. also acknowledge the financial support of the Fundamental Research Funds for the Central Universities.

References

1 I. Ibrahim, I. O. Ali, T. M. Salama, A. A. Bahgat and M. M. Mohamed, *Appl. Catal., B*, 2016, **181**, 389–402.
2 R. M. Abdelhameed, M. El-Shahat and H. E. Emam, *Carbohydr. Polym.*, 2020, **247**, 116695.
3 X.-J. Yang, B. Chen, L.-Q. Zheng, L.-Z. Wu and C.-H. Tung, *Green Chem.*, 2014, **16**, 1082–1086.
4 H.-U. Blaser, H. Steiner and M. Studer, *ChemCatChem*, 2009, **1**, 210–221.
5 R. Liang, F. Jing, G. Yan and L. Wu, *Appl. Catal., B*, 2017, **218**, 452–459.
6 K. Yaemsunthorn, M. Kobielusz and W. Macyk, *Catal. Today*, 2024, **432**, 114598.
7 W. Chen, T. Huang, Y.-X. Hua, T.-Y. Liu, X.-H. Liu and S.-M. Chen, *J. Hazard. Mater.*, 2016, **320**, 529–538.
8 Z. Lv, H. Zhou, H. Liu, B. Liu, M. Liang and H. Guo, *Chem. Eng. J.*, 2017, **330**, 1297–1305.
9 Y. Liu, T. Hu, S. He, L. Feng, Q. Zhao, J. Jiang and L. Wei, *Chem. Eng. J.*, 2023, **477**, 146867.
10 X. Wang, Y. Wang, M. Gao, J. Shen, X. Pu, Z. Zhang, H. Lin and X. Wang, *Appl. Catal., B*, 2020, **270**, 118876.
11 X. Ren, M. Gao, Y. Zhang, Z. Zhang, X. Cao, B. Wang and X. Wang, *Appl. Catal., B*, 2020, **274**, 119063.
12 S. Alismaail, S. H. Ahmed, M. Bakiro and A. Alzamly, *Photochem. Photobiol. Sci.*, 2021, **20**, 997–1009.
13 J. Greeley, T. F. Jaramillo, J. Bonde, I. Chorkendorff and J. K. Nørskov, *Nat. Mater.*, 2006, **5**, 909–913.
14 Y. Huang, Y. Zhu, S. Chen, X. Xie, Z. Wu and N. Zhang, *Adv. Sci.*, 2021, **8**, 2003626.
15 A. Kundu, S. Sharma and S. Basu, *J. Phys. Chem. Solids*, 2021, **154**, 110064.
16 L. Wang, D. Lv, Z. Yue, H. Zhu, L. Wang, D. Wang, X. Xu, W. Hao, S. Dou and Y. Du, *Nano Energy*, 2019, **57**, 398–404.
17 S. Wu, J. Xiong, J. Sun, Z. D. Hood, W. Zeng, Z. Yang, L. Gu, X. Zhang and S.-Z. Yang, *ACS Appl. Mater. Interfaces*, 2017, **9**, 16620–16626.
18 L. Wang, R. Wang, T. Qiu, L. Yang, Q. Han, Q. Shen, X. Zhou, Y. Zhou and Z. Zou, *Nano Lett.*, 2021, **21**, 10260–10266.
19 Y. Zhang, Z. Xu, Q. Wang, W. Hao, X. Zhai, X. Fei, X. Huang and Y. Bi, *Appl. Catal., B*, 2021, **299**, 120679.
20 S. Sun, M. Watanabe, J. Wu, Q. An and T. Ishihara, *J. Am. Chem. Soc.*, 2018, **140**, 6474–6482.
21 X. Li, L. Luo, H. Guo, B. Weng, L. Sun, G. Velpula, I. Aslam, M. B. J. Roeffaers, Q. Chen, L. Zeng, M.-Q. Yang and Q. Qian, *J. Mater. Chem. A*, 2024, **12**, 11841–11847.
22 W. Wang, C. Wen, J. Guan, H. Man and J. Bian, *J. Ind. Eng. Chem.*, 2021, **103**, 305–313.
23 X. Zhao, Y. Xia, X. Wang, N. Wen, H. Li, X. Jiao and D. Chen, *Chem. Eng. J.*, 2022, **449**, 137874.
24 J. Yang, L. Yang, M. Fang, L. Li, F. Fu, H. Xu, M. Li and X. Fan, *J. Colloid Interface Sci.*, 2023, **631**, 44–54.
25 L. Yuan, B. Weng, C. J. Calors, Y. Sun and Y.-J. Xu, *Small*, 2017, **13**, 1702253.
26 K. Zhang, J. Liang, S. Wang, J. Liu, K. Ren, X. Zheng, H. Luo, Y. Peng, X. Zou, X. Bo, J. Li and X. Yu, *Cryst. Growth Des.*, 2012, **12**, 793–803.
27 S. Gong, G. Zhu, R. Wang, F. Rao, X. Shi, J. Gao, Y. Huang, C. He and M. Hojamberdiev, *Appl. Catal., B*, 2021, **297**, 120413.
28 A. Kaur and S. K. Kansal, *Chem. Eng. J.*, 2016, **302**, 194–203.
29 D. Zhu and Q. Zhou, *Appl. Catal., B*, 2020, **268**, 118426.
30 Q. Li, Y. Xia, C. Yang, K. Lv, M. Lei and M. Li, *Chem. Eng. J.*, 2018, **349**, 287–296.
31 A. Chen, X. Li, J. Wang and J. Zhang, *Energy Mater. Adv.*, 2023, **4**, 0028.
32 J. Yu and X. Xu, *Energy Mater. Adv.*, 2022, **2022**, 2692–7640.
33 B. Su, Y. Kong, S. Wang, S. Zuo, W. Lin, Y. Fang, Y. Hou, G. Zhang, H. Zhang and X. Wang, *J. Am. Chem. Soc.*, 2023, **145**, 27415–27423.

34 B. Su, M. Zheng, W. Lin, X. F. Lu, D. Luan, S. Wang and X. W. Lou, *Adv. Energy Mater.*, 2023, **13**, 2203290.
35 B. Alfakes, C. Garlisi, J. Villegas, A. Al-Hagri, S. Tamalampudi, N. S. Rajput, J.-Y. Lu, E. Lewin, J. Sá, I. Almansouri, G. Palmisano and M. Chiesa, *Surf. Coat. Technol.*, 2020, **385**, 125352.
36 G. Ortiz Rabell, M. R. Alfaro Cruz and I. Juárez-Ramírez, *Int. J. Hydrogen Energy*, 2022, **47**, 7770–7782.
37 X. Yue, S. Yi, R. Wang, Z. Zhang and S. Qiu, *Nano Energy*, 2018, **47**, 463–473.
38 R. Chen, L. Meng, C. Wang, W. Xu, Y. Huang, L. Song and L. Li, *SusMat*, 2024, **4**, 154–165.
39 J. Qiu, Q. Zhou, M. Yu, J. Liu, R. Zhuang, Y. Hua, L. Ding and X. Zhang, *SusMat*, 2023, **3**, 894–908.
40 C. Jia, X. Zhang, K. Matras-Postolek, B. Huang and P. Yang, *Carbon*, 2018, **139**, 415–426.
41 K. Darowicki, S. Krakowiak and P. Ślepski, *Electrochim. Acta*, 2006, **51**, 2204–2208.
42 S. Zhang, Y. Yuan, J. Gu, X. Huang, P. Li, K. Yin, Z. Xiao and D. Wang, *Appl. Surf. Sci.*, 2023, **609**, 155446.
43 L. Peng, C. Yu, Y. Ma, G. Xie, X. Xie, Z. Wu and N. Zhang, *Inorg. Chem. Front.*, 2022, **9**, 994–1005.
44 W. Zhou, L. Li, R. Qin, J. Zhu, S. Liu, S. Mo, Z. Shi, H. Fang, P. Ruan, J. Cheng, G. Fu and N. Zheng, *Sci. China: Chem.*, 2022, **65**, 726–732.
45 X. Li, R. Zhu, B. Sun, L. Chen, H. Yang, X. Liu, Y. Guo and Y. Wang, *Chem. Eng. J.*, 2024, **487**, 150652.
46 X. Li, Y. Tan, Z. Liu, J. Su, Y. Xiao, B. Qiao and Y. Ding, *J. Catal.*, 2022, **416**, 332–343.